Atmospheric
Measurement
Techniques

Optical thickness and effective radius of Arctic boundary-layer clouds retrieved from airborne nadir and imaging spectrometry

E. Bierwirth[1], A. Ehrlich[1], M. Wendisch[1], J.-F. Gayet[2], C. Gourbeyre[2], R. Dupuy[2], A. Herber[3], R. Neuber[4], and A. Lampert[4,*]

[1]University of Leipzig, Institute for Meteorology, Leipzig, Germany
[2]Université Blaise Pascal, Laboratoire de Météorologie Physique, Aubière, France
[3]Alfred Wegener Institute for Polar and Marine Research, Bremerhaven, Germany
[4]Alfred Wegener Institute for Polar and Marine Research, Potsdam, Germany
[*]now at: Institute of Aerospace Systems, TU Braunschweig, Germany

Correspondence to: E. Bierwirth (eike.bierwirth@uni-leipzig.de)

Abstract. Arctic boundary-layer clouds in the vicinity of Svalbard (78° N, 15° E) were observed with airborne remote sensing and in situ methods. The cloud optical thickness and the droplet effective radius are retrieved from spectral radiance data from the nadir spot (1.5°, 350–2100 nm) and from a nadir-centred image (40°, 400–1000 nm). Two approaches are used for the nadir retrieval, combining the signal from either two or five wavelengths. Two wavelengths are found to be sufficient for an accurate retrieval of the cloud optical thickness, while the retrieval of droplet effective radius is more sensitive to the number of wavelengths. Even with the comparison to in-situ data, it is not possible to definitely answer the question which method is better. This is due to unavoidable time delays between the in-situ measurements and the remote-sensing observations, and to the scarcity of vertical in-situ profiles within the cloud.

1 Introduction

The Arctic is strongly affected by global warming (Walsh et al., 2011), and clouds play an integral part in these changes (Wu and Lee, 2012). The understanding of Arctic clouds is crucial to predict their role in climate (McBean et al., 2005). The Arctic heating trend (+2 °C since the mid-1960s) was reported to continue in 2011 (Overland et al., 2012) and regionally in 2012 (Overland et al., 2013). The microphysical characteristics of clouds (particle phase, size, concentration, and shape) determine their radiative properties and their impact on the Earth's radiation budget (Curry et al., 1996; Ehrlich et al., 2008a). This is of particular interest in the Arctic where climate change is particularly strong and boundary-layer clouds greatly influence the surface radiation budget, as shown by Shupe and Intrieri (2004) from ground-based remote-sensing observations. In particular, the microphysical characteristics of mixed-phase clouds and their relationships with atmospheric conditions are key questions of cloud physics (Korolev and Isaac, 2006; de Boer et al., 2010; Seifert et al., 2010) that will be addressed by follow-up studies to this paper. This article is a methodological first step toward addressing those issues more extensively.

Problems in retrievals of cloud properties from remote sensing arise both from instrument uncertainty and from assumptions made in the radiative transfer models that are used for the retrieval algorithms (Brest et al., 1997; Marshak et al., 2006). Thus, credible verification of these retrievals requires (i) direct comparison to in-situ measurements; and (ii) comparison of spectral radiances simulated by radiative transfer models to measured radiances (Formenti and Wendisch, 2008; Barker et al., 2011). This is how airborne observations can assist space-borne retrievals, as the aircraft can go back and observe what is inside and underneath the cloud that was remotely sensed. Additionally, satellite observations are often obstructed by the low contrast between clouds and the snow- or ice-covered surface (Krijger et al., 2011). In general, airborne or ground-based cloud observations are scarce, especially over the Arctic Ocean.

For the purpose of improving the data base of the Arctic climate system, the aircraft campaign SoRPIC (Solar Radiation and Phase Discrimination of Arctic Clouds) was conducted in the Norwegian Arctic, including one of the first applications of an AisaEAGLE imaging spectrometer for cloud studies. SoRPIC was a collaboration of the Alfred Wegener Institute for Polar and Marine Research (AWI) in Bremerhaven (Germany), the University of Leipzig (Germany), the Blaise Pascal University of Clermont-Ferrand (France), the Free University of Berlin (Germany) and the German Aerospace Center DLR. The measurement platform was the Polar-5 research aircraft (C-GAWI) of AWI. This Basler BT67 aircraft is a former DC-3 modernised by Basler Turbo Conversion Oshkosh (Wisconsin, USA) with modern avionics, navigation systems and turbo prop engines required for polar research. It was put in service in 2007 (Herber et al., 2008). With an operational range of 1500 km, a maximum altitude of 7.5 km (24 000 feet), 15 kVA of electrical power, and a weight capacity of 2000 kg, the Polar-5 provides a reliable platform for the study of boundary-layer clouds in the Arctic. It is based out of Bremerhaven, Germany, and is presently operated by Kenn Borek Air Ltd., Calgary (Alberta, Canada).

In this paper, we demonstrate the combination of spectral nadir radiances and imaging spectrometry in the retrieval of cloud properties (optical thickness, effective radius) for one flight scenario during SoRPIC. In that field campaign, the upward radiance was measured by several instruments, including a nadir spectrometer and an imaging spectrometer. Our goal is to combine these measurements into a novel retrieval procedure, based on the classic retrieval by Nakajima and King (1990). The classic retrieval uses two wavelengths. It can be improved by including the information from more wavelengths which is available from modern spectrometers. In this study, we proceed in this direction by extending the retrieval algorithm to five wavelengths, as suggested by Twomey and Cocks (1989) and Coddington et al. (2010). Further improvement of the retrievals is possible by including even more spectral information, as shown recently by Coddington et al. (2012). In particular, the analysis of the information content is currently being developed as an important tool for optimising cloud retrievals by Coddington et al. (2012) and King and Vaughan (2012). In addition to using more wavelengths, we want to improve the spatial coverage. For this purpose, we installed a nadir-looking imaging spectrometer with a field-of-view that includes that of an established non-imaging nadir spectrometer with a larger spectral range. Both approaches have their own strengths and weaknesses. A separate problem of cloud retrievals in the Arctic is the existence of bright surfaces (ice and snow). In this study, all measurements were performed above a dark surface (ocean).

In this paper, we proceed as follows: first, the cloud optical thickness and effective radius is retrieved from spectral nadir radiances (wavelengths 350–2100 nm), comparing the results of the two-wavelength (2 WL) approach to the results of the

five-wavelength (5 WL) approach. Second, a field of cloud optical thickness is retrieved from the data from an imaging spectrometer (400–1000 nm). As the cloud effective radius cannot be retrieved without measurements beyond 1000 nm, the effective radius needs to be constrained externally in this retrieval. This means that we have to take an intermediate step to find out how much the choice of that constraint matters. Finally, the retrieval results are compared to cloud properties derived from in-situ sampling of cloud particles, highlighting some of the specific problems of single-aircraft cloud observations (mostly, the difficulty to make concurrent in-situ and remote measurements with a single aircraft). This study focuses on a single case (one measurement flight during SoRPIC) where the conditions were sufficiently well defined to focus on the retrieval performance rather than complications and ambiguities in the cloud field. In particular, the presented case is a cloud layer with known vertical extent, the underlying surface was dark, and the warm temperatures ensured a cloud free of ice particles. While ice particles in clouds were a primary objective of the SoRPIC campaign, their clear absence works in the favour of this particular study.

The measurement set-up is presented in Sect. 2; the meteorological situation during the chosen flight in Sect. 3. Section 4 describes the radiative transfer model, while Sect. 5 deals with the comparison of the 2 WL and the 5 WL approach for nadir radiance. The retrieval is then geometrically extended to imaging spectrometry in Sect. 6. Conclusions are given in Sect. 7.

Finally, a note on the word "hyperspectral": due to historic usage, it is generally associated with imaging. This is likely caused by common terms such as "hyperspectral cube" or "hyperspectral camera". In itself, however, the adjective "hyperspectral" does not relate to any spatial information. It merely emphasises the quality of spectral data that cover a contiguous spectral range, in contrast to "multispectral" data that refer to separated bands (Goetz, 2009).

2   Measurements

The SoRPIC campaign was held in Svalbard (Arctic Norway) between 30 April and 20 May 2010. A total of 13 research flights were conducted out of Svalbard's main settlement, Longyearbyen, with the Polar-5 aircraft over the Greenland, Norwegian and Barents Seas. The aircraft was equipped with a combination of remote-sensing and cloud-particle in-situ instruments, listed in Table 1. Some of the instruments are described in a recent book by Wendisch and Brenguier (2013). The remote-sensing equipment for this study included one active (the Airborne Mobile Aerosol Lidar AMALi; Stachlewska et al., 2010) and three passive systems: the Spectral Modular Airborne Radiation Measurement System (SMART-Albedometer); the imaging spectrometer AisaEAGLE; and an automatically tracking Sun

Table 1. Instrumentation of the Polar-5 aircraft during SoRPIC. Acronyms: AMALi (Airborne Mobile Aerosol Lidar), FSSP (Forward Scattering Spectrometer Probe), CPI (Cloud Particle Imager), AMSSP (Airborne Multi Spectral Sunphoto- and Polarimeter), AIMMS (Advanced Airborne MeasureMent Solutions).

Instrument	Measured Quantity	Unit	Range
SMART-Albedometer	Radiance	$\mathrm{W\,m^{-2}\,nm^{-1}\,sr^{-1}}$	$\lambda = 350\text{–}2100\,\mathrm{nm}$
	Irradiance	$\mathrm{W\,m^{-2}\,nm^{-1}}$	$\lambda = 350\text{–}2100\,\mathrm{nm}$
AisaEAGLE	Radiance	$\mathrm{W\,m^{-2}\,nm^{-1}\,sr^{-1}}$	$\lambda = 400\text{–}1000\,\mathrm{nm}$
AMALi	Extinction Coefficient	$\mathrm{km^{-1}}$	$\lambda = 355\,\mathrm{nm},\ 532\,\mathrm{nm}$
	Cloud Top Height	m	$z = 0\text{–}3\,\mathrm{km}$
FSSP–100	Particle Number Concentration	$\mathrm{cm^{-3}\,\mu m^{-1}}$	$d = 3\text{–}95\,\mu\mathrm{m}$
	Effective Diameter	$\mu\mathrm{m}$	
	Liquid Water Content	$\mathrm{g\,m^{-3}}$	
	Extinction Coefficient	$\mathrm{km^{-1}}$	
Polar Nephelometer	Scattering Phase Function	$\mathrm{W\,sr^{-1}}$	$d = 3\text{–}1000\,\mu\mathrm{m},$ $\theta = 3.5\text{–}169°$
CPI	Particle Number Concentration	$\mathrm{l^{-1}\,\mu m^{-1}}$	$\Delta x = 2.3\,\mu\mathrm{m}$
	Effective Diameter	$\mu\mathrm{m}$	
	Extinction Coefficient	$\mathrm{km^{-1}}$	
	Ice Water Content	$\mathrm{g\,m^{-3}}$	
CANON Camera	RGB Radiance	$\mathrm{W\,m^{-2}\,nm^{-1}\,sr^{-1}}$	$\lambda = (446, 530, 591)\,\mathrm{nm}$
Sun Photometer	Aerosol Optical Thickness	–	$\lambda = 367\text{–}1026\,\mathrm{nm}$
Nevzorov Sonde	Liquid/Total Water Content	$\mathrm{g\,m^{-3}}$	$0.003\text{–}3\,\mathrm{g\,m^{-3}}$
AMSSP	Stokes Vector	$\mathrm{W\,m^{-2}\,nm^{-1}}$	$\lambda = 350\text{–}1000\,\mathrm{nm}$
AIMMS–20	Pressure	hPa	
	Temperature	°C	
	Relative Humidity	%	
	Wind Vector	$\mathrm{m\,s^{-1}}$	
Drop Sondes	Pressure	hPa	
	Temperature	°C	
	Relative Humidity	%	

photometer. The imaging spectrometer AisaEAGLE (manufacturer: Specim Spectral Imaging Ltd., Oulu, Finland) was mounted in a tail pod to measure upwelling radiances $I_{\lambda,\mathrm{E}}^{\uparrow}(t, y)$ as a function of wavelength λ, time t and cross-track distance y (subscript E for AisaEAGLE). The AisaEAGLE measures radiances in the spectral range from 403 nm to 966 nm in 240 channels with a spectral resolution (full width at half maximum) of 2–3 nm. The cross-track field-of-view is 40° wide, divided into 512 spatial pixels (1024 photo diodes with double binning). A dark measurement for the correction of electronic noise and the thermal photo-current in the detector has been performed every five minutes. An exposure time of 10 ms was used. The AisaEAGLE could be operated only during the last three flights of SoRPIC.

During all SoRPIC flights, the upwelling radiance $I_{\lambda,\mathrm{S}}^{\uparrow}(t, y_{\mathrm{n}})$ from the nadir point y_{n} was measured by the SMART-Albedometer (subscript S), which also measured spectral downwelling and upwelling irradiances, $F_{\lambda}^{\downarrow}(t)$ and $F_{\lambda}^{\uparrow}(t)$. The upwelling nadir radiance reflected by the cloud was detected by an optical inlet with a field-of-view (FOV) of 1.5° (Ehrlich et al., 2008b); the irradiance by integrating spheres (Crowther, 1997). Fibre optics bring the collected photons to grating spectrometers (manufactured by Zeiss, Jena/Germany; cf. Bierwirth et al., 2009) with 1280 channels for wavelengths from 350 to 2100 nm. An exposure time of 500 ms was used. The spectral resolution of the spectrometers is 2–3 nm at wavelengths below 1000 nm, and 12–15 nm at longer wavelengths. The dark signal is accounted for by dark reference pixels in the spectrometers up to 1000 nm wavelength and by regular dark measurements with opto-mechanical shutters for the near-infrared spectrometers (950–2100 nm). The viewing geometry for the radiances measured by both instruments (AisaEAGLE and SMART-Albedometer) is visualised in Fig. 1. The data processing of the imaging data is illustrated in Fig. 2 along with an example spectrum.

Both the AisaEAGLE and the SMART-Albedometer have their own Inertial Navigation System (INS) that records the aircraft attitude (roll, pitch, and heading angles). Using these attitude data, the optical inlets of the SMART-Albedometer are actively stabilised horizontally to correct for changes of the aircraft attitude of up to 6° with an accuracy of 0.2° (Wendisch et al., 2001). The AisaEAGLE was fixed to the fuselage, so the real-time attitude angles have to be taken into account in data analysis.
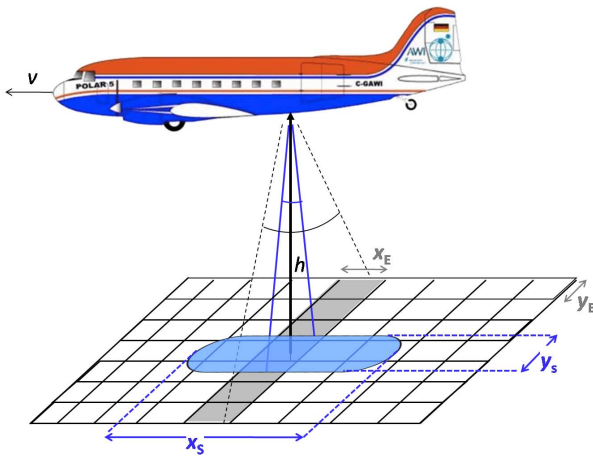
Fig. 1. Viewing geometry for radiances from the Polar-5 aircraft with the field-of-view of the imaging spectrometer AisaEAGLE (black) and of the SMART-Albedometer (blue). Typical dimensions in this study: distance aircraft–cloud $h = 2600$ m, aircraft speed $v = 70$ m s^{-1}, width of one AisaEAGLE pixel $y_E = 3.5$ m, length $x_E = y_E + v \cdot t_E = 4.2$ m with the exposure time $t_E = 10$ ms, width of instantaneous SMART-Albedometer field-of-view $y_S = 68$ m, length due to exposure time $t_S = 0.5$ s: $x_S = y_S + v \cdot t_S = 103$ m.

The AisaEAGLE and the SMART-Albedometer were calibrated in the laboratory with a NIST-traceable standard bulb for irradiances and radiances (combined with a panel of standard reflectivity) and also with a NIST-traceable integrating sphere for radiances. The calibration stability during the field campaign was monitored with a portable integrating sphere, and was better than 3 %. The final radiometric uncertainty is given as 8 % for the AisaEAGLE and 9 % for the SMART-Albedometer radiance, which is mostly due to the uncertainty of the reference standards. The radiometric calibration of AisaEAGLE has been verified by comparing the upwelling radiances with that of the well-established SMART-Albedometer (compare Ehrlich et al., 2012). Using the INS attitude records, the AisaEAGLE pixels that are located in the field-of-view of the SMART-Albedometer radiance sensor are identified for each time step. In this paper, such pixels are referred to as ES pixels (the overlap is shown in Fig. 1). The mean value of all ES pixels is used for comparing AisaEA-GLE and SMART-Albedometer radiance data, as in Fig. 3 for a wavelength of 870 nm. The linear correlation coefficient in Fig. 3 is 0.97; the differences can be attributed not only to the measurement uncertainty, but also to the different time resolution (1–2 Hz for the SMART-Albedometer, 35 Hz for the AisaEAGLE).

The cloud-top altitude was determined from the lidar backscatter signal of AMALi with an altitude resolution of 7.5 m. The in-situ instrumentation includes the Forward Scattering Spectrometer Probe, FSSP–100 (Dye and Baumgardner, 1984), a polar nephelometer (Gayet et al., 1997), and the Cloud Particle Imager, CPI (Lawson et al., 1998, not operational on the flight on 17 May 2010).
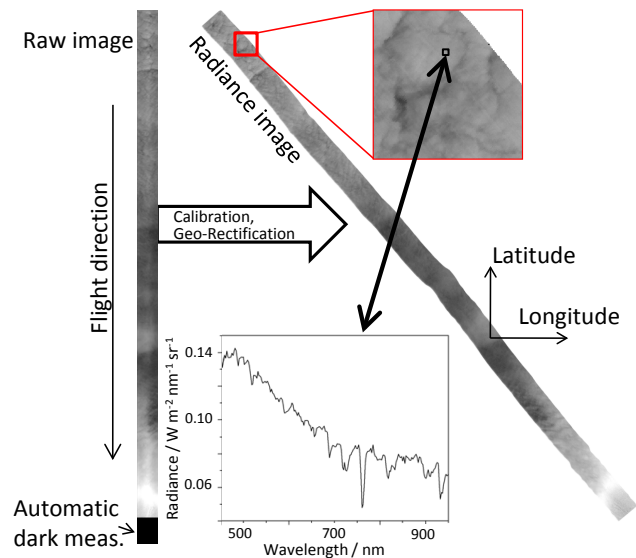

Fig. 2. Data processing of the AisaEAGLE imager. The raw image (left) in digital numbers (0–4095) is completed by an automatic dark measurement every five minutes. The radiometric calibration transforms the digital numbers into radiances. The geo-rectification projects each pixel of the image into the Earth reference system (longitude, latitude). Each pixel contains a full radiance spectrum.

3   The meteorological situation on 17 May 2010

On 17 May 2010, a warm front approached Svalbard from Scandinavia with unusually high temperatures of up to 14 °C (Fig. 4). The warm, dry air (50 % relative humidity) was advected onto a ridge of about 0 °C which remained at the ocean surface under an inversion. As observed by AMALi and the drop sondes (Fig. 5), both the inversion and the cloud top increased in altitude toward north. The maximum temperature ranged from 14 °C at 800 m altitude (74.5° N) to 8 °C at 1200 m (75.9° N). A cloud layer formed in the inversion. We observed from the aircraft that these clouds had a foggy appearance and reached down to the ocean surface. This is supported by the Bjørnøya sounding (50 km west of the southern end of the flight track) that reports continuous saturation up to 400 m (Dietzsch, 2010). An additional higher cloud layer at 1500 m was observed to the north of the warm airmass. That region has been excluded from the following analysis.
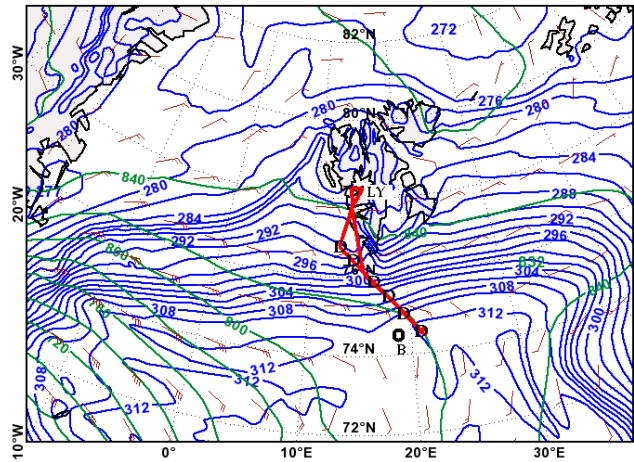
The aircraft flew southward at 3100 m altitude almost parallel to the temperature gradient (Fig. 4), descended at the southernmost point, and headed back north inside the cloud along the same track. Six drop sondes were launched during the southbound leg. Their data can be trusted only below 2900 m after their adjustment to ambient conditions. AMALi could detect only the cloud top due to saturation. All data in this paper stem from flight sections over the open ocean (no snow or sea ice at the surface).
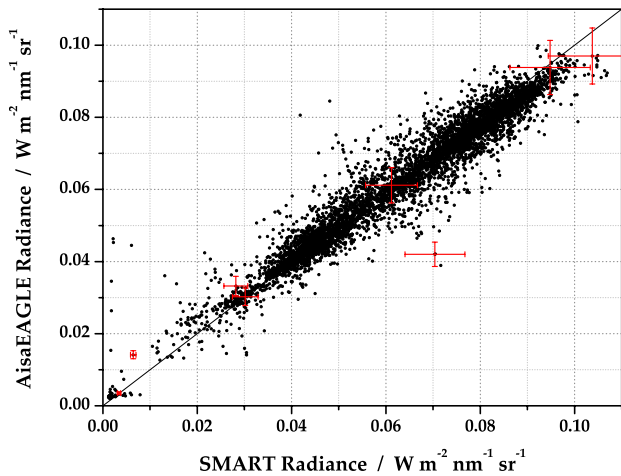
Fig. 3. Comparison of the 870 nm radiance from the SMART-Albedometer and from the SMART spot of the AisaEAGLE for the flight on 17 May 2010. The radiometric uncertainty (8 % for AisaEAGLE, 9 % for SMART-Albedometer) are marked with red crosses at exemplary data points.


Fig. 4. ECMWF analysis chart (925 hPa, 12:00 UTC) and SoRPIC flight track (in red) on 17 May 2010, from Longyearbyen (LY) to 50 km east of Bjørnøya (B) and back. Dropsondes were launched at the D symbols. The contours are the geo-potential height in m (green) and the equivalent potential temperature in K (blue).

4   Radiative transfer modelling

The cloud properties are retrieved from measured radiances from nadir and imaging spectrometry aboard the Polar-5 aircraft. The measured data are checked against look-up tables (LUT) of simulated radiances. These look-up tables are produced with the radiative transfer package libRadtran (Mayer and Kylling, 2005). The radiative transfer calculations are initialised to represent the environmental parameters during the particular SoRPIC flight. That includes the relative geometry of the Sun, the cloud layer and the aircraft; the aerosol optical thickness (AOT) as observed by the Sun photometer; and the cloud-top height which is obtained from the AMALi lidar. The surface AOT was relatively high on 17 May 2010, with a value of 0.25 at 500 nm, while the AOT at 3 km altitude was the background value of 0.1. As aerosol information other than the optical thickness have not been measured, the aerosol type is assumed as OPAC Arctic (Hess et al., 1998) in the calculations. The profiles of atmospheric gases are provided by libRadtran (Anderson et al., 1986, subarctic winter). They are modified to match the meteorological profiles from the drop sondes (the standard profiles are scaled to ensure a continuous transition from the standard table to the drop-sonde data). Drop-sonde data are discarded down to the level where the temperature reading has dropped from cabin to ambient temperature and has started to rise again as the sonde falls into warmer layers. The surface albedo is set to that of open ocean, as all measurements presented here have been performed over ice-free water. The optical properties of the cloud particles are calculated from Mie theory, as the warm temperatures of this case rule out the existence of ice crystals.

The look-up tables then contain the calculated values for the spectral upward radiance. They are given as a function of optical thickness τ and droplet effective radius r_{eff} of a plane-parallel cloud. τ is varied from 0 to 38, r_{eff} is varied from 4 to 18 μm. From the look-up table, the most likely combination of τ and r_{eff} is obtained by interpolating the measured radiance at different wavelengths into the simulated radiance grid. In general, the retrieval runs through five iteration loops. In each step, τ or r_{eff} are alternately retrieved with the other quantity fixed. This ensures a stepwise approximation along the non-orthogonal branches of the retrieval grid. With respect to the choice of wavelengths, different approaches are applied and are described in more detail in the following sections.

The forward model error is calculated as suggested by L'Ecuyer et al. (2006). For each value of cloud optical thickness and effective radius, uncertain model input parameters are varied to a reasonable degree (typically the measurement uncertainty or the natural variability of that parameter). The forward model error is defined as

$$\epsilon = \sqrt{\sum_i \left(\frac{\delta I_i}{I_{\text{ref}}} \right)^2}, \tag{1}$$

where δI_i is radiance variation caused by the variation of error source i, and I_{ref} is the reference radiance from the undisturbed control run. ϵ is a measure of the "noise" generated by the model uncertainties. The error sources are quantified as follows: the atmospheric profiles of humidity and temperature are varied by the amount of natural variability along the flight track, 40 % and 6 °C, respectively (which is much larger than the measurement uncertainties specified by the manufacturer Vaisala: 2 % of relative humidity and 0.2°C).
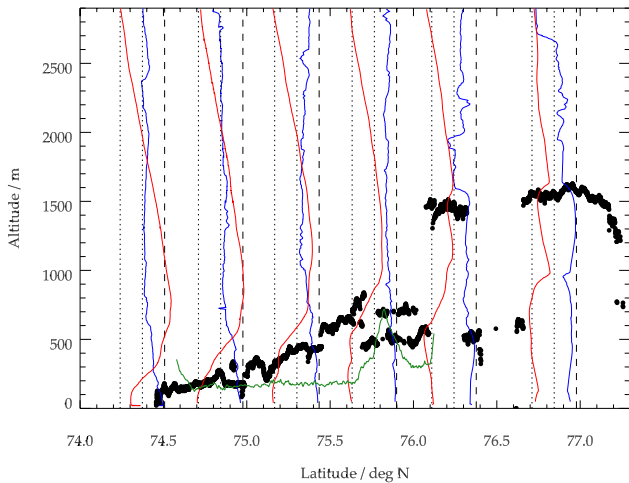
Fig. 5. Illustration of the flight on 17 May 2010. Remote sensing was performed at 3100 m altitude (the top border of the plot), flying southward from 09:00 to 10:22 UTC. After the descent, in-situ observations were performed northward along the green line from 10:39 to 11:21 UTC. Cloud top as detected by the lidar is indicated in black. Cloud bottom was at the ocean surface. Six dropsondes were launched, their profiles are drawn in red (temperature) and blue (relative humidity). Each drop-sonde profile is marked with one dashed and two dotted lines; the dashed lines are placed at the location of the launch, and also represent a temperature of 12 °C and 100 % RH. The central dotted lines show 6 °C and 50 %, the left dotted lines show 0 °C and 0 %.

The surface albedo and the aerosol optical thickness are varied by 10 %. Another error source is the uncertainty of the radiance measurement.

The calculated values of ϵ are dominated by the measurement uncertainty of radiance (9 % for the SMART-Albedometer). All other error sources lead to a slight increase to 9.5 % at the most. Only for cases with $\tau = 0$, the forward model error ϵ was significantly increased to up to 18 %. The contributions of all error sources for the five wavelengths are given in Table 2.

5 Retrieval of cloud properties from nadir radiance

Two approaches have been followed to retrieve the cloud optical properties (optical thickness, effective radius) from spectral nadir radiance measurements by the SMART-Albedometer. First, the two-wavelength approach (2 WL) presented by Nakajima and King (1990) is used with radiances at 515 nm and 1625 nm. The grid of pre-calculated radiances I_{LUT} is interpolated to the actual measured radiance I_{meas} at these wavelengths. Second, a five-wavelength (5 WL) residual approach presented by Coddington et al. (2010) is followed. The same look-up tables are used, but analysed at five wavelengths of 515, 745, 870, 1015, 1240 and 1625 nm in terms of the residuum ζ^2:

$$\zeta^2 = \sum_{i=1}^{5} \left[(5-i)^2 \cdot (I_{i,\text{meas}} - I_{i,\text{LUT}})^2 \right.$$
$$\left. + (i-1)^2 \cdot \left(\frac{I_{i,\text{meas}}}{I_{0,\text{meas}}} - \frac{I_{i,\text{LUT}}}{I_{0,\text{LUT}}} \right)^2 \right], \tag{2}$$

where the index i runs over the five wavelengths in increasing order. The index "meas" indicates measured quantities; the index "LUT" indicates values taken from the look-up table. The weighting factors in Eq. (2) reflect the wavelength dependence of the radiance sensitivity to optical thickness (first term) and effective radius (second term). Each of the five wavelengths represents a different order of magnitude of the bulk absorption coefficient of liquid water and, adding the dependence on droplet size, different ranges of single-scattering albedo (Coddington et al., 2010, Fig. 2). For any given flight geometry, ζ^2 is calculated for all elements of the corresponding look-up table. The minimum indicates the most likely values of r_{eff} and τ. In order to propagate the radiance measurement uncertainty into the retrieved quantity, both retrievals are repeated for the upper and the lower end of the radiance uncertainty range.

The retrieval results are shown in Fig. 6 for optical thickness τ_S and in Fig. 7 for the effective radius r_{eff}^S. In the case of optical thickness, the uncertainty (propagated from the radiance measurement into τ_S space) behaves similarly for both retrieval approaches. As the difference between the two retrieval approaches lies within that uncertainty, we conclude that either approach can be used to retrieve the optical thickness, and the inclusion of additional wavelengths does not provide additional information.

The retrieval of r_{eff}^S is more differentiated. The uncertainties for both approaches differ significantly, with 5 WL yielding lower uncertainties (less than 1 μm) than 2 WL (1–2 μm). With values between 0 and 4 μm, the difference in r_{eff}^S between 5 WL and 2 WL is close to and sometimes exceeds the retrievals' uncertainties. The additional wavelengths increase the retrieval sensitivity of the effective radius. The FSSP data (shown as red line in Fig. 7) are close to the retrieved value in the southern section of the flight, and deviate more strongly from the retrieval starting at and north of 75° N. There are two reasons for this: the time difference between in-situ observations and remote sensing is smaller in the south; and the in-situ observations occurred near the cloud top south of 75° N, while further north the cloud top grew higher above the aircraft and the in-situ observations came from a location deeper inside the cloud. The vertical profile of the cloud droplet size and its impact on remote sensing was studied, for example, by Platnick (2000). For our case, the FSSP observations during the one profile flown at 75.8° N indicate that the liquid water content increased linearly (from 0.07 to 0.2 g m^{-3} in the top half of the cloud). The effective radius derived from the FSSP data was rather constant for the top half of the cloud (10–11 μm), dropping to 6 μm in the lower

Table 2. Forward model errors ϵ (in percent) at the five retrieval wavelengths for different error sources: surface albedo (varied by 10 %), aerosol optical thickness AOT (10 %), temperature T (6 K), relative humidity RH (±40 %). The total includes the measurement uncertainty for radiance (9 %). Values in parentheses are for the case $\tau = 0$.
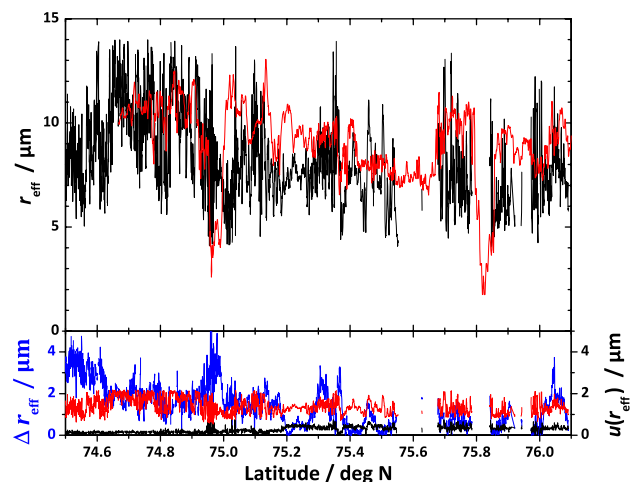
Source	ϵ_{515}	ϵ_{745}	ϵ_{870}	ϵ_{1015}	ϵ_{1625}
Albedo	0.0–0.5 (2.0)	0.0–0.7 (4.3)	0.0–0.7 (5.5)	0.0–0.7 (6.4)	0.0–0.7 (7.1)
AOT	1.6–2.8 (0.9)	0.9–1.5 (1.8)	0.8–1.1 (3.3)	0.8 (4.5)	0.7–0.8 (5.4)
T	0.1–0.5 (1.9)	0.0–0.7 (4.5)	0.0–0.8 (5.7)	−0.2–0.6 (6.5)	0.0–0.8 (7.4)
RH-	−1.0–1.7 (6.3)	−0.4–1.8 (9.8)	−0.6–1.2 (9.4)	0.1–1.6 (11)	−0.3–1.1 (10)
RH+	−2.1––0.2 (−4.4)	−1.3––0.3(-2.8)	−0.4––0.1 (0.4)	−0.6 (2.1)	−0.6––0.4 (4.1)
Total	9.2–9.5 (11)	9.1–9.3 (15)	9.1–9.2 (16)	9.0–9.2 (17)	9.0–9.2 (18)
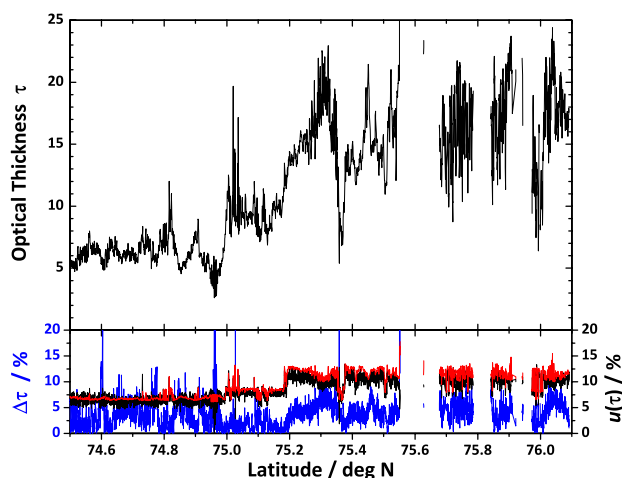
Fig. 6. Top panel: cloud optical thickness τ in aircraft nadir retrieved from the SMART-Albedometer radiance by 2 WL. Bottom panel: relative difference $\Delta\tau$ between τ retrieved by 2 WL and 5 WL (blue); propagated uncertainty $u(\tau)$ in 5 WL (black) and 2 WL (red), in percent.


Fig. 7. Cloud-particle effective radius r_{eff} in aircraft nadir retrieved from the SMART-Albedometer radiance. Top panel: r_{eff} retrieved by 2 WL (black) and observed by the FSSP (red) at the same latitude, but one hour later. Bottom panel: absolute difference Δr_{eff} between 2 WL and 5 WL (blue); propagated uncertainty $u(r_{\text{eff}})$ in 5 WL (black) and 2 WL (red).

half (about one third of the geometric cloud thickness; lower levels could not be sampled due to flight safety concerns). This indicates that contributions from different penetration depths would not skew the apparent effective radius as seen from above, as long as contributions from the lower cloud half are negligible.

The retrieved $r_{\text{eff}}^{\text{S}}$ for 2 WL and 5 WL are compiled in Fig. 8 in the form of two histograms, one for the flight section north of 75° N and one for the section south of 75° N. Figure 8 shows that 2 WL and 5 WL yield similar distributions of r_{eff} for the northern section, and both deviate equally from the in-situ observations that occurred deeper in the cloud. On the other hand, 2 WL and 5 WL do not agree for the southern flight section, and the distribution from the FSSP observations near cloud top lies between the both. The 5 WL retrieval reports a larger amount of large droplets, while 2 WL prefers lower values. Judging by the lower retrieval uncertainty of 5 WL, the larger values would seem more realistic; however, the deviation from the in-situ distribution is beyond

the FSSP uncertainty of 1 μm. Therefore, it is impossible to validate neither 2 WL nor 5 WL with independent measurements, with the time delay between remote sensing and in-situ observations being the most likely source of uncertainty.

6 Retrieval of cloud properties from imaging spectrometry

The retrieval of the cloud properties from imaging spectrometry uses the same principles as the retrieval from the radiance in the nadir spot. The benefit of the imaging data is that they include off-track pixels, adding another dimension not only to the measured data, but also to the look-up tables (viewing angle). However, the AisaEAGLE does not cover wavelengths longer than 1000 nm. Therefore, the effective radius cannot be retrieved for the off-track pixels of the AisaEAGLE because wavelengths shorter than 1000 nm
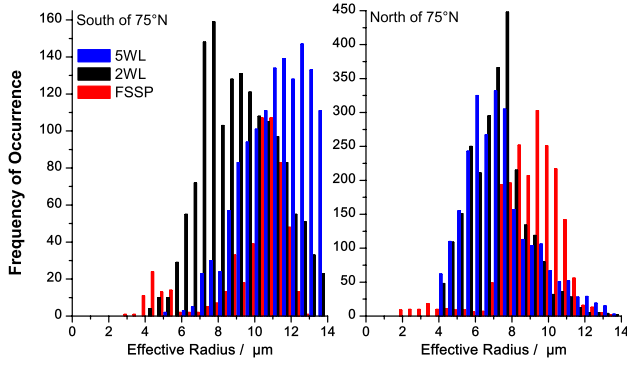
Fig. 8. Histograms showing the effective radius retrieved from the SMART-Albedometer radiance by 5 WL (blue) and 2 WL (black) and as observed by the FSSP (red) at the same latitude, but one hour later. Left: for the flight section south of 75° N. Right: north of 75° N.
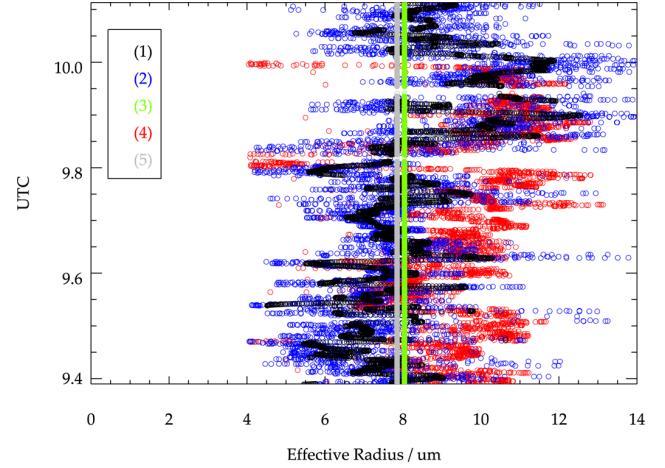

Fig. 9. Time series for the five different choices of the effective radius used as a constraint in the retrieval of the optical thickness from the imaging data.

are sensitive almost only to the optical thickness. In the following, the cloud optical thickness τ_E is retrieved from the 870 nm radiances for each pixel in the field-of-view of the AisaEAGLE. For this purpose, the retrieval grid by Nakajima and King (1990) was constrained to a fixed value of the effective radius, r_{eff}^{fix}. This value is taken from other measurements on the same flight. As there are several options to choose this constraint of the effective radius, we first tested the sensitivity of the retrieval to this choice.

6.1 Influence of effective radius

As we have no information about the effective radius in the off-track pixels, we make a basic assumption in the choice of the fixed value r_{eff}^{fix}: the cloud-particle statistics in this stratiform cloud layer is the same in the x (flight) and y (across-track) directions. Our first option for the effective radius is a moving average of the retrieval from the SMART-Albedometer, $r_{eff}^{fix}(t) = r_{eff}^{(1)}(t) = \langle r_{eff}^S(t - \Delta t/2, t + \Delta t/2) \rangle$. Here, the averaging period Δt is obtained as follows: first, the width d of the observed strip of cloud is determined from the height h between cloud top and the aircraft (which we know from the lidar) and the AisaEAGLE's field-of-view ($\alpha_E = 40°$). Then the nadir effective radii $r_{eff}^S(t)$ from the SMART-Albedometer are averaged over the time in which the radiance spot on the cloud top has travelled a distance that is equal to d, so

$$d = v \cdot \Delta t + 2h \cdot \tan(\alpha_S/2), \qquad (3)$$

with α_S being the viewing angle of the radiance inlet, Δt the averaging time, and v the aircraft speed (ignoring any cloud motion with the assumption $v \gg v_{cloud}$). The last term in Eq. (3) adds the radiance field-of-view behind and in front of the nadir point. Hence, the averaging time interval

is $[t - \Delta t/2, t + \Delta t/2]$ with

$$\Delta t = \frac{2h}{v} \cdot \left(\tan \frac{\alpha_E}{2} - \tan \frac{\alpha_S}{2} \right). \qquad (4)$$

The other options for the choice of the effective radius include instantaneous and averaged values from remote sensing (S) or from in situ (index i). The complete list is this:

1. The moving average in nadir, $r_{eff}^{(1)}(t) = \langle r_{eff}^S(t - \Delta t/2, t + \Delta t/2) \rangle$;

2. the current effective radius in nadir, $r_{eff}^{(2)}(t) = r_{eff}^S(t)$;

3. the mean effective radius of the entire flight leg, $r_{eff}^{(3)} = \langle r_{eff}^S(t) \rangle \, \forall t$;

4. the value measured by in-situ instruments at the same location x, $r_{eff}^{(4)}(t) = r_{eff}^i(x^i = x^S(t))$, where x^i is the aircraft location during the in-situ measurements and x^S during the remote-sensing leg;

5. the mean value of all in-situ measurements, $r_{eff}^{(5)} = \langle r_{eff}^i(x^i) \rangle \, \forall x^i$.

All five options for r_{eff}^{fix} are used as a constraint to derive the optical thickness for all off-track AisaEAGLE pixels. Their values are compared in Fig. 9. This results in a spread of the retrieved optical thickness τ_{ES} in the ES pixels of 0.3–0.4 units of optical thickness, which is less than the retrieval uncertainty.

The histograms of the entire field of optical thickness retrieved with the five different constraints of effective radius (Fig. 10) show that the choice matters only in one case and when the optical thickness is less than 8. That choice, $r_{eff}^{(4)}$, leads to a significantly lower frequency of such low values
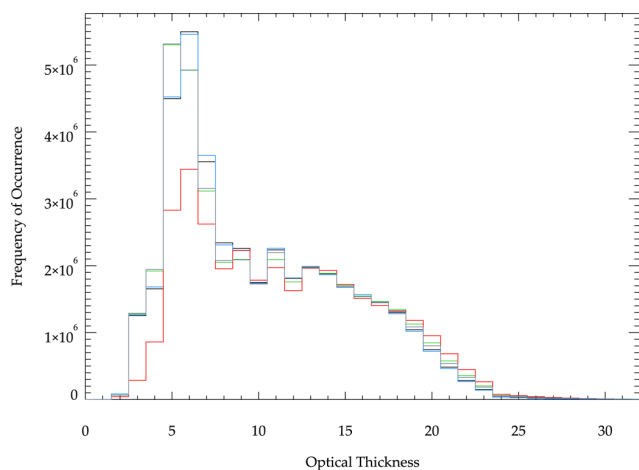
Fig. 10. Histogram of the optical thickness retrieved with different constraints of the effective radius. (1) black, (2) blue, (3) green, (4) red, (5) grey.

Fig. 11. Map of the cloud optical thickness as retrieved from radiances measured by the AisaEAGLE on 17 May 2010 at 10:14 UTC. The red curve shows true nadir, the blue lines delineate the field-of-view of the SMART-Albedometer radiance. The depicted cloud field is 2 km wide and 1 km long. Each pixel shows a cloud area of 4 m width.

of optical thickness, while the other choices are consistent among each other. This may be due to the fact that the radiance even at short wavelengths is not purely a function of cloud optical thickness, but also of effective radius (the non-orthogonality of the retrieval grid). Another plausible reason lies in the definition of $r_{\text{eff}}^{(4)}$ which implies that the cloud is still there and the same when it is probed the second time (the first time being the remote sensing, the second time the in situ flight leg). This is not likely to be the case. In the time between both visits, the cloud may have evolved or moved, and local inhomogeneities gain importance. Thin parts of the cloud (with low optical thickness) would be particularly affected by local turbulence, which is in line with Fig. 10. Summarising, we conclude that with the possible exception of $r_{\text{eff}}^{(4)}$ the choice of the constraining effective radius has little significance to the retrieval of the cloud optical thickness.

6.2 Retrieval results

The retrieval from imaging data of the AisaEAGLE results in a map of the retrieved cloud optical thickness. An example is shown in Fig. 11. This map has been drawn such that the aircraft nadir (marked with the red line) is always in the centre. The wavy edge of the map represents the rolling of the aircraft during the flight. The ES pixels that are observed by the SMART-Albedometer radiance surround the nadir point and are delineated by the blue lines. The cloud structure is clearly visible. The black-and-white colour scale makes Fig. 11 resemble a photograph of the same scene, because clouds appear white and open ocean appears black to the human eye. Nevertheless, Fig. 11 does in fact not include any information about the ground surface underneath the cloud.
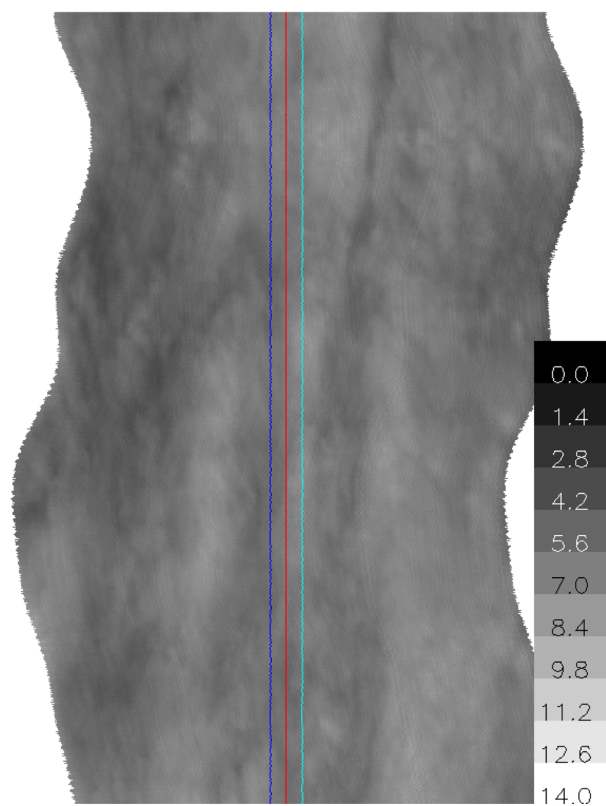
The following statistics of the cloud properties for 17 May are based on the retrieval that uses the current effective radius $r_{\text{eff}}^{(2)}(t)$ from the SMART-Albedometer. The look-up tables are calculated for a range of values of solar zenith angle, relative azimuth angle, viewing zenith angle, and cloud-top height. They are then interpolated to the particular conditions of each measurement point. The remaining look-up table contains radiances as a function only of viewing angle and cloud optical thickness. The viewing angle is fixed for each pixel of the camera and is modified by the aircraft roll angle. So for each pixel, the modelled radiance is only a function of τ, and the radiance measured in this pixel yields the retrieved τ value for that point. For the flight on 17 May, a total of 4×10^7 values have been retrieved; see the histogram in Fig. 12.

The histograms for the entire field-of-view and for the ES pixels do not differ significantly, which justifies the assumption that the cloud statistics are the same in flight direction and across (on the scale of the field-of-view). The distribution of the cloud optical thickness as retrieved from the imaging spectrometer is similar to that retrieved from
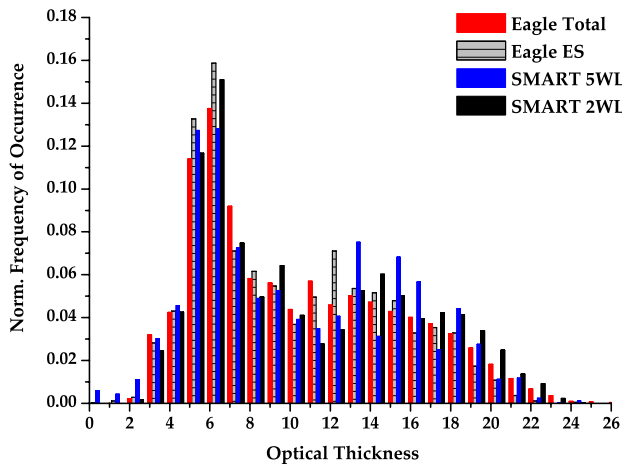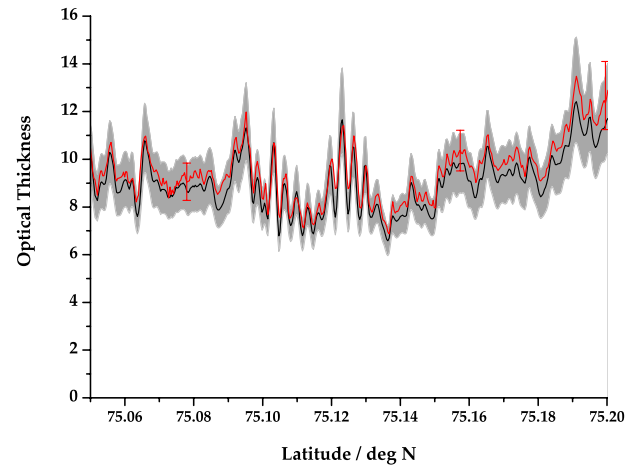
Fig. 12. Histogram of the cloud optical thickness retrieved from radiances measured by the AisaEAGLE in all spatial pixels (red) and in the nadir (ES) pixels (gray), compared to the optical thickness retrieved from nadir radiances measured by the SMART-Albedometer (5 WL algorithm in blue, 2 WL in black).

Fig. 13. Time series (excerpt) of the average cloud optical thickness in the ES pixels of the AisaEAGLE (black, with uncertainty range in grey), compared to that retrieved from the SMART-Albedometer radiance (red, with uncertainty range indicated by exemplary error bars).

the nadir radiances of the SMART-Albedometer, although the AisaEAGLE provides about 20 times more data points. Only the ES pixels can be directly compared to the simultaneous retrieval by the SMART-Albedometer in nadir. A time series is shown in Fig. 13. The optical thickness retrieved from nadir radiances (red line) agrees within the grey-shaded range of uncertainty with the optical thickness retrieved from the ES pixels of the imaging spectrometer.

7 Conclusions

We have shown that airborne measurements of the spectral nadir radiance can be successfully combined with imaging spectrometry to retrieve the cloud optical thickness as a two-dimensional field as wide as the field-of-view (40°). Besides the geometric expansion of the available data, we have also worked towards a better exploitation of the spectral information contained in our measurements. The classic retrieval approach uses two wavelengths. In this paper, we have compared that to a five-wavelength algorithm, while parallel works by Coddington et al. (2012), King and Vaughan (2012), and Werner et al. (2013) point out that the full spectral information as well as the usage of wavelength ratios can ultimately be used to optimise retrievals. This present paper takes two steps: (1) applying retrievals that use two and five wavelengths to nadir measurements of spectral radiance to retrieve the cloud optical thickness and effective radius; and (2) extending the geometric coverage for optical thickness to a 40° field-of-view by incorporating imaging spectrometry (also called hyperspectral imaging) into the algorithm. Step (2) lacks a retrieval of effective radius due to limited spectral coverage of the imaging spectrometer.

Both the two-wavelength (2 WL) and the five-wavelength (5 WL) approach have been applied to retrieve the cloud optical thickness and effective radius from the nadir radiances of the SMART-Albedometer. While the two approaches agree within uncertainty for the optical thickness, they differ in respect to effective radius: 5 WL seems to be more sensitive to larger droplets (more than 10 μm radius) than 2 WL. However, even with the comprehensive instrumentation that was deployed in the SoRPIC campaign, including state-of-the-art remote sensing and in-situ instrumentation, it is impossible to give a definite answer to the question which of the two methods yields better results. Fundamental limitations are the time delay between remote sensing and in-situ observations as well as the vertical variability of the microphysics within the cloud. Only with simultaneous collocated measurements above and inside the cloud (with two aircraft) can this limitation be overcome and can closure between the different methods be achieved. The aircraft within the cloud would alternate between profiling (to capture the general vertical structure of the cloud) and flight legs near cloud top for closure purposes. A measurement campaign to this purpose is currently being prepared.

We used imaging spectrometry to retrieve the cloud optical thickness in a 40° field-of-view across the flight track at 4 m resolution. This extends the application of the imaging spectrometer AisaEAGLE to airborne cloud research, and shows the potential of this rapidly developing technology. Figure 11 demonstrates how the two-dimensional cloud statistics become available with imaging spectrometry. First, it allows us to compare the statistics along the flight track (as observed by a single radiance sensor, such as the SMART-Albedometer) to the statistics across the flight track. This will

be particularly useful in cases of non-stratiform or undulating cloud fields. Furthermore, such a highly-resolved spatial distribution of the cloud optical thickness gives us the opportunity to feed a very realistic cloud field into a Monte Carlo model of radiative transfer. The spatial extent of the model domain can be increased by a meandering flight pattern to cover a large rectangular area (provided that the flying speed is faster than cloud evolution). Additionally, cases of three-dimensional photon interactions between a heterogeneous surface albedo and a cloud layer can be investigated. For instance, imagine a single ice floe in the middle of Fig. 11. While the retrieval of the cloud optical thickness would become more complicated, the observed radiance field would be very valuable to study how radiation reflected by the ice floe propagates within the cloud. Furthermore, that behaviour likely depends on the distribution of ice particles inside a mixed-phase cloud. In a similar fashion, cloud edges can be observed at high spatial resolution. With the added benefit of a full spectrum, imaging spectrometry of clouds can be a powerful tool to study adjacency and cloud-edge effects.

With our current instrumentation used during SoRPIC, the retrieval of cloud properties from imaging spectrometry is limited to the retrieval of cloud optical thickness, because the AisaEAGLE does not cover the wavelengths required for a retrieval of the effective radius. However, compatible imagers for those wavelengths already exist and could be successfully applied to additionally retrieve the effective radius.

References

Anderson, G. P., Clough, S. A., Kneizys, F. X., Chetwynd, J. H., and Shettle, E. P.: AFGL Atmospheric Constituent Profiles (0–120 km), Tech. Rep. AFGL-TR-86-0110, Air Force Geophys. Lab, Hanscom Air Force Base, Bedford, MA, USA, 1986.

Barker, H. W., Jerg, M. P., Wehr, T., Kato, S., Donovan, D. P., and Hogan, R. J.: A 3D cloud construction algorithm for the Earth-CARE satellite mission, Q. J. Roy. Meteorol. Soc., 137, 1042–1058, 2011.

Bierwirth, E., Wendisch, M., Ehrlich, A., Heese, B., Tesche, M., Althausen, D., Schladitz, A., Müller, D., Otto, S., Trautmann, T.,

Dinter, T., von Hoyningen-Huehne, W., and Kahn, R.: Spectral surface albedo over Morocco and its impact on radiative forcing of Saharan dust, Tellus B, 61, 252–269, 2009.

Brest, C. L., Rossow, W. B., and Roiter, M. D.: Update of Radiance Calibrations for ISCCP, J. Atmos. Ocean. Tech., 14, 1091–1109, 1997.

Coddington, O. M., Pilewskie, P., Redemann, J., Platnick, S., Russell, P. B., Schmidt, K. S., Gore, W. J., Livingston, J., Wind, G., and Vukicevic, T.: Examining the impact of overlying aerosols on the retrieval of cloud optical properties from passive remote sensing, J. Geophys. Res., 115, D10211, doi:10.1029/2009JD012829, 2010.

Coddington, O. M., Pilewskie, P., and Vukicevic, T.: The Shannon information content of hyperspectral shortwave cloud albedo measurements: Quantification and practical applications, J. Geophys. Res., 117, D04205, doi:10.1029/2011JD016771, 2012.

Crowther, B.: The Design, Construction, and Calibration of a Spectral Diffuse/Global Irradiance Meter, Ph.D. thesis, University of Arizona, Tucson, AZ, USA, 1997.

Curry, J. A., Rossow, W. B., Randall, D., and Schramm, J. M.: Overview of Arctic cloud and radiation characteristics, J. Climate, 9, 1731–1764, 1996.

de Boer, G., Hashino, T., and Tripoli, G. J.: Ice nucleation through immersion freezing in mixed-phase stratiform clouds: Theory and numerical simulations, Atmos. Res., 96, 315–324, 2010.

Dietzsch, F.: Charakaterisierung der synoptischen Situation während der Kampagne SORPIC April/Mai 2010, B.S. Thesis, University of Leipzig, Germany, 2010.

Dye, J. E. and Baumgardner, D.: Evaluation of the Forward Scattering Spectrometer Probe. Part I: Electronic and Optical Studies, J. Atmos. Ocean. Tech., 1, 329–344, 1984.

Ehrlich, A., Wendisch, M., Bierwirth, E., Herber, A., and Schwarzenböck, A.: Ice crystal shape effects on solar radiative properties of Arctic mixed-phase clouds–Dependence on microphysical properties, Atmos. Res., 88, 266–276, 2008a.

Ehrlich, A., Bierwirth, E., Wendisch, M., Gayet, J.-F., Mioche, G., Lampert, A., and Heintzenberg, J.: Cloud phase identification of Arctic boundary-layer clouds from airborne spectral reflection measurements: test of three approaches, Atmos. Chem. Phys., 8, 7493–7505, doi:10.5194/acp-8-7493-2008, 2008b.

Ehrlich, A., Bierwirth, E., Wendisch, M., Herber, A., and Gayet, J.-F.: Airborne hyperspectral observations of surface and cloud directional reflectivity using a commercial digital camera, Atmos. Chem. Phys., 12, 3493–3510, doi:10.5194/acp-12-3493-2012, 2012.

Formenti, P. and Wendisch, M.: Combining upcoming satellite missions and aircraft activities, B. Am. Meteorol. Soc., 89, 385–388, 2008.

Gayet, J. F., Crépel, O., Fournol, J. F., and Oshchepkov, S.: A new airborne polar Nephelometer for the measurements of optical and microphysical cloud properties. Part I: Theoretical design, Ann. Geophys., 15, 451–459, doi:10.1007/s00585-997-0451-1, 1997.

Goetz, A. F. H.: Three decades of hyperspectral remote sensing of the Earth: A personal view, Remote Sens. Environ., 113, S5–S16, 2009.

Herber, A., Dethloff, K., Haas, C., Steinhage, D., Strapp, J. W., Bottenheim, J., McElroy, T., and Yamanouchi, T.: POLAR 5 – a new research aircraft for improved access to the Arctic, in: Extended Abstracts of the First International Symposium on the Arctic Re-

search (ISAR-1), Miraikan, Japan, 4–6 November 2008, 54–57, 2008.

Hess, M., Koepke, P., and Schult, I.: Optical properties of aerosols and clouds: The software package OPAC, B. Am. Meteorol. Soc., 79, 831–844, 1998.

King, N. J. and Vaughan, G.: Using passive remote sensing to retrieve the vertical variation of cloud droplet size in marine stratocumulus: An assessment of information content and the potential for improved retrievals from hyperspectral measurements, J. Geophys. Res., 117, D15206, doi:10.1029/2012JD017896, 2012.

Korolev, A. and Isaac, G. A.: Relative Humidity in Liquid, Mixed-Phase, and Ice Clouds, J. Atmos. Sci., 63, 2865–2880, doi:10.1175/JAS3784.1, 2006.

Krijger, J. M., Tol, P., Istomina, L. G., Schlundt, C., Schrijver, H., and Aben, I.: Improved identification of clouds and ice/snow covered surfaces in SCIAMACHY observations, Atmos. Meas. Tech., 4, 2213–2224, doi:10.5194/amt-4-2213-2011, 2011.

Lawson, R. P., Korolev, A. V., Cober, S. G., Huang, T., Strapp, J. W., and Isaac, G. A.: Improved measurements of the drop size distribution of a freezing drizzle event, Atmos. Res., 47–48, 181–191, 1998.

L'Ecuyer, T. S., Gabriel, P., Leesman, K., Cooper, S. J., and Stephens, G. L.: Objective Assessment of the Information Content of Visible and Infrared Radiance Measurements for Cloud Microphysical Property Retrievals over the Global Oceans. Part I: Liquid Clouds, J. Appl. Met. Clim., 45, 20–41, 2006.

Marshak, A., Platnick, S., Várnai, T., Wen, G., and Cahalan, R. F.: Impact of three-dimensional radiative effects on satellite retrievals of cloud droplet sizes, J. Geophys. Res., 111, D09207, doi:10.1029/2005JD006686, 2006.

Mayer, B. and Kylling, A.: Technical note: The libRadtran software package for radiative transfer calculations – description and examples of use, Atmos. Chem. Phys., 5, 1855–1877, doi:10.5194/acp-5-1855-2005, 2005.

McBean, G., Alekseev, G., Chen, D., Forland, E., Fyfe, J., Groisman, P. Y., King, R., Melling, H., Vose, R., and Whitfield, P. H.: Arctic Climate: Past and Present, in Arctic Climate Impact Assessment, edited by: Symon, C., Arris, L., and Heal, B., 21–60, Cambridge University Press, New York, USA, 2005.

Nakajima, T. and King, M.: Determination of the Optical Thickness and Effective Particle Radius of Clouds from Reflected Solar Radiation Measurements. Part I: Theory, J. Atmos. Sci., 47, 1878–1893, 1990.

Overland, J., Bhatt, U., Key, J., Liu, Y., Walsh, J., and Wang, M.: Temperature and Clouds [in Arctic Report Card 2011], available at: http://www.arctic.noaa.gov/reportcard, last access: 11 July 2012.

Overland, J., Key, J., Kim, B.-M., Kim, S.-J., Liu, Y., Walsh, J., Wang, M., and Bhatt, U.: Air Temperature, Circulation and Clouds [in Arctic Report Card 2012], available at: http://www.arctic.noaa.gov/reportcard, last access: 24 January 2013.

Platnick, S.: Vertical photon transport in cloud remote sensing problems, J. Geophys. Res., 105, 22919–22935, 2000.

Seifert, P., Ansmann, A., Mattis, I., Wandinger, U., Tesche, M., Engelmann, R., Müller, D., Pérez, C., and Haustein, K.: Saharan dust and heterogeneous ice formation: Eleven years of cloud observations at a central European EARLINET site, J. Geophys. Res., 115, D20201, doi:10.1029/2009JD013222, 2010.

Shupe, M. D. and Intrieri, J. M.: Cloud radiative forcing of the Arctic surface: The influence of cloud properties, surface albedo, and solar zenith angle, J. Climate, 17, 616–628, 2004.

Stachlewska, I. S., Neuber, R., Lampert, A., Ritter, C., and Wehrle, G.: AMALi – the Airborne Mobile Aerosol Lidar for Arctic research, Atmos. Chem. Phys., 10, 2947–2963, doi:10.5194/acp-10-2947-2010, 2010.

Twomey, S. and Cocks, T.: Remote Sensing of Cloud Parameters from Spectral Reflectance in the Near-Infrared, Beitr. Phys. Atmosph., 62, 172–179, 1989.

Walsh, J. E., Overland, J. E., Groisman, P. Y., and Rudolf, B.: Ongoing climate change in the Arctic, Ambio, 40, 6–16, doi:10.1007/s13280-011-0211-z, 2011.

Wendisch, M. and Brenguier, J.-L. (Eds.): Airborne Measurements for Environmental Research: Methods and Instruments, Wiley-VCH Verlag GmbH & Co. KGaA, Weinheim, Germany, 2013.

Wendisch, M., Müller, D., Schell, D., and Heintzenberg, J.: An airborne spectral albedometer with active horizontal stabilization, J. Atmos. Ocean. Tech., 18, 1856–1866, 2001.

Werner, F., Siebert, H., Pilewskie, P., Schmeissner, T., Shaw, R. A., and Wendisch, M.: New airborne retrieval approach for trade wind cumulus properties under overlying cirrus, J. Geophys. Res. Atmos., online first, doi:10.1002/jgrd.50334, 2013.

Wu, D. L. and Lee, J. N.: Arctic low cloud changes as observed by MISR and CALIOP: Implication for the enhanced autumnal warming and sea ice loss, J. Geophys. Res., 117, D07107, doi:10.1029/2011JD017050, 2012.